Multiple remote sensing assessment of the catastrophic collapse in Langtang Valley induced by the 2015 Gorkha Earthquake

Hiroto Nagai[1], Manabu Watanabe[2], Naoya Tomii[3], Takeo Tadono[1], Shinichi Suzuki[1]

[1]Earth Observation Research Center, Japan Aerospace Exploration Agency, 2-1-1 Sengen, Tsukuba, Ibaraki, 305-8505, Japan
[2]School of Science and Engineering, Tokyo Denki University, Ishizaka, Hatoyama-machi, Hiki-gun, Saitama, 305-0394, Japan
[3]Satellite Applications and Operations Center, Japan Aerospace Exploration Agency, 2-1-1 Sengen, Tsukuba, Ibaraki, 305-8505, Japan

Correspondence to: Hiroto Nagai (nagai.hiroto@jaxa.jp)

Abstract. The main shock of the 2015 Gorkha Earthquake in Nepal induced numerous avalanches, rockfalls, and landslides in Himalayan mountain regions. A major village in the Langtang valley was destroyed with numerous victims by a catastrophic avalanche event, which consists of snow, ice, rock, and blast wind. The hazard process is understood mainly depending on limited witness, interview, and an in-situ survey after a monsoon season. To record immediate situation and to understand deposition process, we performed an assessment by means of satellite-based observations carried out in no later than two weeks after the event. The avalanche-induced sediment deposition was delineated with calculation of decreasing coherence and visual interpretation of amplitude images acquired from the Phased Array-type L-band Synthetic Aperture Radar-2 (PALSAR-2). These outlines area highly consistent with that delineated from a high-resolution optical image of WorldView-3 (WV-3). The delineated sediment areas were estimated as 0.63 km^2 (PALSAR-2 coherence calculation), 0.73 km^2 (PALSAR-2 visual interpretation), and 0.88 km^2 (WV-3), respectively. In the WV-3 image, surface features were classified into 10 groups. Our analysis suggests that the avalanche event contains a sequence of (1) fast splashing body with air blast, (2) muddy huge mass flowing, (3) less mass flowing from another source, (4) smaller amount of splashing and flowing mass, and (5) splashing mass without flowing at the east and west sides. By means of satellite-derived pre- and post-event digital surface models, differences in the surface altitudes of the collapse events estimated the total volume of the sediments as $5.51 \pm 0.09 \times 10^6$ m^3, most mass of which are distributed along the river floor and a tributary water stream. These findings contributes for detail numerical simulation of the avalanche sequences as well as source identification, and furthermore, altitude measurements after ice/snow melting would reveal a contained volume of melting ice and snow.

Keywords. ALOS-2, InSAR, WorldView-3, ALOS World 3D, avalanche, Nepal, Himalaya

1 Introduction

A great earthquake of 7.8 Mw, namely the 2015 Gorkha Earthquake, occurred in the district of Lamjung, central Nepal on April 25, 2015 (Ge et al. 2015; Parameswara et al. 2015), which caused more than 9,000 deaths and 23,000 people to be injured (e.g., Roy et al. 2015). Damages in urban areas were especially caused on stone/brick masonry structures (Goda et al. 2015), whereas numerous landslides were induced in rural/mountain areas (ICIMOD 2015a; Kargel et al. 2015).

The most catastrophic collapse in the mountainside was reported in the Langtang valley, located 70 km north of Kathmandu (ICIMOD 2015b; Kargel et al. 2015). Landslides, avalanches, and sudden air pressure wave traveled from a south-facing steep slope to the bottom of a U-shaped valley. The fallen materials, i.e., a mass of boulders, snow, and ice, covered the valley bottom involving almost all the buildings in Langtang Village. At the opposite side of the valley, trees were prostrated and lost their leaves by the sudden air pressure wave. More than 170 villagers (reaching its double including trekkers and porters) were killed (or left missed) in this event.

Generally, damage detection through Synthetic Aperture Radar (SAR) technique has ever been applied for urban damaged areas (e.g., Kobayashi et al, 2011; Yonezawa and Takeuchi, 2001; Tamura and El-Gharbawi, 2015; Watanabe et al., 2016), but almost no case for a large-scale mountain hazard was studied. Therefore we apply SAR damage detection for this event. Fragmentary information from witness, interview, and in-situ survey after a monsoon season give some clues, however scientific understanding of the avalanche process is still poor. Detailed interpretation of the sediment deposition by means of immediately-observed high-resolution optical satellite imagery coupled with sediment volume estimation would provide comprehensive spatial and volumetric distribution and a temporal sequence of material deposition. In this study, therefore, we carry out (1) the identification with SAR for urgent response, (2) the mapping and interpretation of the deposition sequence with high-resolution optical imagery, and (3) the volume estimation using the difference between pre- and post-event digital surface models (DSMs). These results lead to evaluate SAR application for mountain hazard response and to discuss the overall picture of the avalanche.

2 Data set and Processing

2.1 Study site

The catastrophic collapse was caused in the middle of Langtang Valley (28º12'50"N, 85º30'5"E), one of the national parks in Nepal (Fig. 1). The main river in this valley, the Langtang Khola, flows from the east to the west, and joins the main stream, Bote Kosi (Trisuli Gandaki), at the end of the valley near a village, Syabru Bensi (Ono and Sadakane 1986). The length of the valley is approximately 50 km, and the width ranges from 1 to 2 km. A typical U-shaped valley formed by glaciation. The Lirung, Khyimjung, Yala, Shalbachum, Langtang, and Langshisa glaciers are located 4100 m above sea level (a.s.l.). In addition, several unnamed glaciers are distributed along both the ridges of the U-shaped valley (Shiraiwa and Watanabe 1991), where Mt. Langtang Lirung is the highest peak (7239 m a.s.l.).

The Lantang valley consists of the Gosainkund gneiss zone (various gneisses and granitic migmatite) and the Langtang Himal migmatite zone (medium-grained garnet-mica-gneiss of granitic composition and coarse-grained augen-gneiss) (Arita et al. 1973; Shiraiwa and Watanabe 1991). Six successive glacial stages were recognized from an in-situ dating survey on moraine compositions (Shiraiwa and Watanabe 1991; Shiraiwa, 1994). Relatively extensive glaciation in the Langtang Stage (3650–3000 yr BP) is suggested in the late Quaternary. Permafrost is not highly expected in this valley because of the large amount of winter snow, which prevents deep freezing in winter (Shiraiwa, 1994).

The Langtang Valley is a famous trekking course for tourists, and it has been called "one of the most beautiful valleys in the world." The village of Langtang was called "Yul" by the villagers (Ono and Sadakane 1986). The main local occupations are farming and tourism. Many temporary houses called "Kalkha" were built around the village for livestock farming, i.e., for the transhumance of yaks.

2.2 Avalanche event

In this catastrophic event, co-seismic snow-and-ice avalanches and rockfalls with concurrent air blasts (Cadwalladr 2015). This contains multiple phenomena as described as "disaster-within-a-disaster" (Kargel, 2015). The sediment deposition is consists mostly of accumulated snow and less dominantly of glacier ice (Fujita et al. 2016). Satellite-based thermal infrared observation on 5 days after the quake denoted the deposition has 10-20 K lower surface temperature than surrounding terrains (Kargel et al. 2016). Water stream of the Langtang river was blocked once by the deposition but quickly recovered as the ice-and-snow deposition was melted (Kargel et al. 2016). The materials near the river bed had less boulder and sand-rich deposition, suggesting that they are originated from snow avalanche (Fujita et al. 2016). From the sediment volume and catchment area on the mountain hill, original snow depth before the avalanche occurrence was estimated at 1.82 m in the catchment hillslopes (Fujita et al. 2016). A meteorological observation at a neighbouring glacier suggested four major

snowfall events since Oct 2014 and an anomalous large amount of snow was charged before the quake. An interview reported that many hanging glaciers were cracked and huge pieces of ice falling occurred forming a cloud gathering snow and rocks with air blast (Cadwalladr 2015). However an in-situ survey suggested that detached glacier ice was less dominant than involved snow, represented by observed clear ice balls in the deposition (Fujita et al. 2016). After an following mas movement between 8 and 10 May, ice-and-snow melting decrease the sediment volume by 40% until Oct, 2015 (Fujita et al. 2016).

Multiple landslides was also reported (Cadwalladr 2015). Ice cliffs, exposure of ice-rich thick layer under a bolder-rich debris layer, are identified near the Langtang river, suggesting different timing of avalanche and subsequent rockfalls (Fujita et al. 2016). In the opposite-side north-facing steep slopes, debris materials were found at 200-m higher places above the deposition bottom, which suggested that they travelled at 63 m s^{-1} (Kargel et al. 2016). On the other hand, avalanche entraining sand and silt was reported as “black avalanches” (Fujita et al. 2016). Post-event photographs and satellite images suggested debris materials originated from rockfall and landslide were not dominant in the deposition (Fujita et al. 2016; Kargel et al. 2016).

The related articles all reported trees fallen down to uniformed directions at the opposite-side north-facing slope (Cadwalladr 2015; Fujita et al. 2016; ICIMOD 2015; Kargel et al. 2016). This was caused by catastrophic air blast reaching 332 km h^{-1} travelled up to neighbouring villages of Singdum and Mundu (Kargel et al. 2016). Location change of a boulder over the event suggest that it received a blast exceeding 50 m s^{-1} (Fujita et al. 2016).

In terms of collapse trigger, three separated main sources were suggested around the mountain peaks at 7000 m a.s.l. by snow cover thinning (~20 m) between April 2014 and May 2015 (Lacroix 2016). Hanging glacier detachment was considered by another study (Fujita et al. 2016). As described above, furthermore, anomalous winter snow seemed to amplify the sediment mass (Fujita et al. 2016). Topographic comparisons over the event revealed that the total mass of the sediment deposition was $6.81 \pm 1.54 \times 10^6$ m^3 before the second mass movement caused in 8-10 May (Fujita et al. 2016) and 6.95×10^6 m^3 including the second mass deposition (Lacroix 2016)

2.2 Synthetic aperture radar imagery

In order to estimate the damages after the earthquake on April 25, the Japan Aerospace Exploration Agency carried out an emergency observation with the Phased Array type L-band Synthetic Aperture Radar-2 (PALSAR-2) onboard the Advanced Land Observing Satellite-2 (ALOS-2, "DAICHI-2") aiming central Nepal at 7:02 on April 26 (GMT). This image was taken on the left-looking strip-map mode with a 3-m spatial resolution along the descending orbit of Path 55. Visual interpretation of the orthorectified backscatter amplitude image of HH polarization (product level 2.1) was performed. A pre-event PALSAR-2 image taken at 6:13 on December 28, 2014 was used for comparison. This image was taken in a right-looking strip-map mode with a 3-m spatial resolution along the descending orbit of Path 48. Visual interpretation of the orthorectified backscatter amplitude image of HH polarization (product level 2.1) was simultaneously performed.

Not only the amplitude imagery but also the phase information emitted and received by the synthetic aperture radar (SAR) contributes to the situational awareness. We performed coherence calculation using interferometric phase information of SAR, which was explained by Plank (2014) in detail. Coherence can be calculated from two SAR images observing an identical place twice from the same orbit and incidence angle, thereby achieving similar phase and intensity information of the receiving microwave, which is calculated for a pair of SAR images by

$$\gamma = \frac{E\langle c_1 c_2^* \rangle}{\sqrt{E\langle c_1 c_1^* \rangle E\langle c_2 c_2^* \rangle}} \quad (1)$$

where c_1 and c_2 are the corresponding complex-valued pixels of the two images, c* is the complex conjugate of c, and E indicates the expected value. The detailed mathematical procedure is described in Touzi et al. (1999) and López-Martínez and Pottier (2007). A significant change in surface feature between two observations results in lower coherence (in other

words, lower similarity). Other noisy influences, including vegetation growth, can be reduced by calculating normalized differences with a coherence calculated from two pre-hazard images. The normalized coherence decrease (NCD) is calculated as

$$\gamma_{diff} = \frac{\gamma_{pre} - \gamma_{\text{int}}}{\gamma_{pre} + \gamma_{\text{int}}} \quad (2)$$

where γ_{pre} is the coherence value between two images before the earthquake (October 4, 2014 and February 21, 2015), and γ_{int} is the coherence value between the two images over the earthquake (February 21 and May 2, 2015). These data were acquired from a same orbit with a spatial resolution of 10 m. When γ_{int} is calculated for images over a hazard, higher-valued pixels of γ_{diff} indicate the reduction of the similarity, which has high potential of hazard-induced deformation or destruction. Several previous studies applied this method using L-band SAR for damage detection in urban areas (e.g., Kobayashi et al., 2011; Yonezawa and Takeuchi, 2001; Tamura and El-Gharbawi, 2015; Watanabe et al., 2016), but no such study applied this method for mountain hazard. Throughout this study, we aim to emphasize the possibility of normalized conference difference by using L-band SAR for damage detection in mountain regions.

Numerous noises are removed by focal statistics. In the NCD raw image, all pixel values are overwritten by the mean values within 15-pixel circles around each pixel (Fig. 2). This filter emphasizes the concentration of high values, whereas the homogeneously scattered high values are de-emphasized. The detailed steps are as follows:

1. The radius of a window circle is set as 15 pixels.
2. A mean value of the pixels in a circle is calculated.
3. The mean value is placed in the center pixel of the circle.
4. Moving the circle, every pixel on the output image is filled with the mean values in the same way.

2.3 Pre-event optical imagery and DSM

Pre-event optical satellite imagery and its three-dimensional view were generated to grasp the previous situation in further details. Images of the Panchromatic Remote-sensing Instrument for Stereo Mapping (PRISM) and the Advanced Visible and Near Infrared Radiometer type 2 (AVNIR-2) onboard the Advanced Land Observing Satellite (ALOS) were acquired at 5:02 on October 12, 2008, which were combined into a orthorectified pan-sharpened image. It is a visible color image with a spatial resolution of 2.5 m. A DSM dataset "ALOS World 3D (AW3D)" was used for this study. AW3D was generated from numerous (>3 million scenes) PRISM nadir, forward, and backward images, which were taken through ALOS operation period (2006 to 2011), automatically stacked, and synthesized into a global DSM dataset with a horizontal spacing of 5 m (Tadono et al., 2015). In addition to its finer resolution than existing datasets such of the Suttle Radar Topography Mission (SRTM) and the Global Digital Elevation Model by Advanced Spaceborne Thermal Emission and Reflection Radiometer (ASTER GDEM) (larger than 30 m), occasional anomaly values was excluded in the generation process as well as occasional cloud cover filled with other scenes. As a result, an accuracy of 4.10 m root mean square for the vertical component versus globally distributed ground control points (4622 points) was reported (Tadono et al., 2015). The orthorectified pan-sharpened image was overlain on the AW3D DSM with a pixel spacing of 5 m to show a three-dimensional view for interpretation.

2.4 Post-event optical imagery and DSM

Post-event optical satellite imagery and DSM were used to recognize the damaged situation in detail. A DigitalGlobe's satellite, WorldView-3 (WV-3) observed the Langtang valley on May 8, 2015, with a panchromatic sensor of 0.31 m spatial resolution and a multispectral sensor of 1.24 m spatial resolution to generate a set of pan-sharpened stereo pair imagery (Fig. 3). First, Area of Interest (AOI) is defined as that includes all sediment depositions. The complicated sediment outlines are

delineated from the WV-3 near-infrared band, which appears the best clear contrast between the sediment depositions and the surface terrain, by means of a segmentation function of Iterative Self Organizing (ISO) cluster classifier in ArcGIS (e.g. Ball and Hall, 1965; Richards and Richards) (Fig. 4a). Other multispectral band images (Red, Green, and Blue) and the panchromatic image are synthesized into a pan-sharpened image (i.e. color imagery with 0.3-m spatial resolution). Using this image, the sediment depositions are divided into several groups based on visible characteristics of colors (dark or light) and deposition features (splashing, muddy, and flowing) (Figs. 4b-4f). After all the steps these images and delineated polygon layers are orthorectified with 174 tie points onto the ALOS pan-sharpened image taken on October 12, 2008.

Using the set of pan-sharpened stereo pair imagery, on the other hand, a post-event DSM in a pixel spacing of 2 m was produced by NTT DATA as its commercial service. The DSM is generated by stereo photogrammetric method using two WV-3 images acquired on May 8, 2015 using stereo-area-collect mode (26.2 km swath, 112 km path). Two images that are (1) forward looking with cross-track tilting to the west hand (i.e., average off-nadir angle: 27º, average target azimuth: 245º /scene id: 104001000BA62E00) and (2) backward looking with cross-track tilting to the west hand (i.e., average off-nadir angle: 27º, average target azimuth: 319º /scene id: 104001000B3B2300) were acquired. Spatial resolution after cross-track tilt was 0.38 m, coarsened from 0.31 m because of tilting. DSM generation flow (i.e., stereo matching, RPC ortho-rectification, pixel resampling, and DSM data output) was performed by NTT DATA with their original software, where the geo-referencing process was supported by WV-3 accurate orbit information without any in-situ ground control point and a resampled pixel spacing of 2 m. Officially announced specification shows a vertical accuracy of 4 m and a horizontal accuracy of 5 m as root mean square errors. In two sites that are neighboring the sediment surface, relative calibration/validation of this DSM and the AW3D DSM was performed and summarized in a supplementary material, in which a standard deviation error of 1.5 m between WV-3 and AW3D DSM is reported.

3 Results

3.1 SAR amplitude imagery

A post-event PALSAR-2 backscatter amplitude image is shown in Fig. 5a, and a pre-event image is shown in Fig. 5b. The brightness of these images corresponds to the amplitude of microwave signal reflected to the PALSAR-2 antenna. The difference between the two represents a completely modified surface feature. The mass of the sediment is identifiable only in the post-event image within an area of 0.73 km^2 (centroid: 28º12’54”N, 85º30’14”E), ranging approximately 1500 m from the upstream to the downstream of the Langtang Khola and 700 m from the upper to the bottom part of the U-shaped valley. Comparing the pre-event PALSAR-2 backscatter amplitude image (Fig. 5b) and an ALOS PRISM/AVNIR-2 pan-sharpened image taken on October 12, 2008 (Fig. 5c), bright points and a valley-shaped feature correspond to buildings and water streams, respectively. These features completely disappear in Fig. 5a, which means that they have been filled by the sediment mass after the quake. A three-dimensional view of the ALOS PRISM/AVNIR-2 image overlaid on the AW3D DSM is shown in Fig. 5d. This sediment area is located below the terminus of a glacier on the north-facing slope. Another glacier flows toward the debris-covered area of the former glacier. This geography suggests a possibility that a large volume of materials travelled from these glaciers with an extremely high potential energy.

3.2 SAR coherence decrease

NCD is calculated from the PALSAR-2 images (Fig. 6a). NCD values greater than 0.2 are reclassified into multiple colours with 0.05 steps, in which scattered NDC dots are difficult to be identified. After a focal statistics process with the 15-pixel circle, noisy pixels were moderated and several parts with a high NCD appeared (Fig. 6b). One of the high-value areas (>0.2) correspond to the sediment outline delineated from the PALSAR-2 amplitude image (p in Fig. 6b). Separated from a connecting upper outline at the narrowest part (< 5-pixel width), this part has an area of 0.63 km^2 with a centroid of

[28º12'57"N; 85º30'14"E]. Visual interpretation of the amplitude images (Fig. 5) and NCD calculation (Fig. 6) yield a similar result for the collapsed sediments (Fig. 6b). Moreover, the both methods are not hindered by the cloudy weather, and hence, have a great potential to immediately indicate a catastrophic collapse and contribute to decision-making for such hazards in the monsoon season.

Furthermore, above the sediment mass, two parts on the south-facing slope show high-NCD concentrations in (q) 0.22 km^2 and (r) 0.07 km^2 areas (Fig. 6b). They are located at the downstream periphery of the Glacier Termini, suggesting the consequent collapse from the tributary glacier to the main glacier. High NCD does not appear on the glacier surfaces possibly because frequent avalanches and glacier flows cause regular changes in the surface. For such surfaces, the changes uniquely caused by an earthquake could be identified by NCD calculation.

3.3 Collapse mapping with a post-event optical imagery

Visual identification and mapping of the sediment depositions from the very-high-resolution WV-3 image resulted in 0.88 km^2 covering which was classified into 10 groups (A-J) (Fig. 3; Table 1). The group (A) (area: 0.16 km^2) is characterized by dark muddy bottom to splashing uphill parts (Fig. 4b) where numerous trees fallen to the splashing direction are identified as previous studies reported (Fig. 4c) (e.g. Kargel et al. 2015). The group (B) (area: 0.25 km^2) begins from the headwall just under a glacier with relatively lighter colour than (A) (Figs. 4b; 4d). It flows to the river floor with curved streaks (Figs. 3; 4d; 4e). In the river flow, it shows more mud-like feature with visible wrinkles as group (C) (area: 0.13 km^2), accumulating to the downstream and slightly to the upstream, maintaining the same colour (Fig. 4b). The group (D) (area: 0.14 km^2) basically has clearly darker surface than (B) and (C) with less streaks and several splashed patches (Fig. 4e). Simultaneously gradual colour transition is seen from (D) to (B) (Fig. 4e). The group (E) (area: 0.02 km^2) is located at the lower side of (D) with the same colour and rather muddy feature quite like (C) (Fig. 4e). Gradual colour transition is also seen from (D) to (B). On the east side, very dark-colour patches of (F) (area: 0.02 km^2) and detached parts (G) (area: 0.01 km^2) are found (Figs. 3). They seem splashing, but have relatively muddy feature and not so homogeneous directivity compared to (A). Dark aperture deposition of (H) (area: 0.07 km^2) begins from another headwalls which is wider than and is independent from that for (B) (Fig. 4f). The splashing parts are blocked by (B) and (C), whereas the western part starts flowing along a narrow path to the river floor grouped as (I) (area: 0.02 km^2) (Fig. 3). This flow is finally connected to and covers (C) (Fig. 4c). The group (J) (area: 0.05 km^2) is a parallel and more aperture/splashing deposition compared to (H) (Fig. 4f). The surface colour varies from lighter to darker than (J), not related to the flow path.

3.4 Surface elevation changes

According to the relative calibration/validation of the AW3D and WV-3 DSMs (see the Supplementary material), A horizontal offset of 5 m (1 pixel) to the east and an altitude offset of –27.0 m were added to the WV-3 DSM to meet the AW3D DSM with the best consistency. Possible altitude error of 1.5 m was given to calculate uncertain volumes. After the calibration, the difference between the post-event WV-3 DSM and the pre-event AW3D DSM was calculated and illustrated (Fig. 7a; Table1). An example of vertical profile shows sediment deposition in entire surface terrain from the foot of the head wall to the river floor, followed by altitude decrease on the steep vegetated slope (Fig. 7b), whereas another profile shows main deposition most mainly at the river floor (Fig. 7c).

The spatial distribution of altitude change classified into the 10 sediment groups revealed an increase in surface altitude in the collapse site reaching a maximum of 46.4 m in the group (C) (Table 1). The increase in the altitude was especially pronounced in the groups (C) (mean: 17.8 m) and (E) (mean: 19.7 m), which are muddy depositions located along the river bed. Altitude decreasing was denoted in the groups (A), (F), and (G), where dominance of surface erosion and DSM error are considered. Mean altitude changes in the groups (D), (H), and (J) are smaller than the defined uncertainty level, 1.5 m.

Calculating the altitude change and surface area, a total deposition volume of $5.51 \pm 0.09 \times 10^6$ m^3 was estimated, which is included within the estimated volume range by Fujita et al. (2016) ($6.81 \pm 1.54 \times 10^6$ m^3) and not larger than the volume including the second mass movement (6.95×10^6 m^3) (Lacroix 2016). In addition, total eroded volume of $1.64 \pm 0.06 \times 10^6$ m^3 was estimated, most of which belongs to the group (A). In addition to the effect of the fallen trees, fundamental bias error induced by WV-3 DSM generation is considered for this extremely steep slope, because splashed patches and muddy deposition both denotes negative values. As well, groups (F) and (G) have negative net volume difference, possibly because of building collapse and slightly negative DSM bias larger than the deposition volume of the dark-colour materials.

4 Discussion

4.1 SAR-derived surface changes

The sediment outline delineated from the PALSAR-2 amplitude image has an area of 0.73 km^2, which is very close (i.e. contained area difference smaller than 5%) to what Kargel et al. (2015) measured, which slightly underestimates what the WV-3 high-resolution image suggested (0.88 km^2). Hazard scale is thus able to be known similarly by the methods. The outline delineated from the PALSAR-2 image (0.63 km^2) reaches 86% of the area obtained from the WV-3 image (Fig. 8). Its spatial coverage corresponds to the groups (B) to (F) and parts of (G) and (J). Most of the flowing parts are included in that coverage, whereas splashed parts beside the central body are excluded (Fig. 8). It suggests that splashed materials are difficult to be recognized with a 3-m spatial resolution of PALSAR-2 imagery. Furthermore, the group (A) on the north-facing slopes is also ignored. Possibly, the microwave reflection from/to PALSAR-2 was hindered by the very steep mountain hillslope.

The sediment outline extracted by NCD calculation has an area of 0.63 km^2, which is 72% of that from the WV-3 image. Its spatial coverage corresponds to the groups (B), (D), (F), (G) and small parts of (A) and (H). NCD indication on the coverage between (F) and (G) can be explained if the surface materials before the avalanche were extensively blown away (e.g., from vegetation or buildings to bare terrain). No NCD indication along the riverbed is explainable by the geomorphic alternation constitutively caused by the river erosion, which de-emphasizes the avalanche-caused change in the NCD index. North-facing slopes were covered by forestry, where little NCD is explainable owing to growing trees and seasonal defoliation. Two extra parts of high NCD value caused on the valley bottom (i.e. villages of Chyamki and Singdum) ((s) in Fig. 6b) are corresponding to other collapse occurrences which were identifiable with an optical image shown in Fig. S6c of Kargel et al. (2015).

The geospatial information derived from PALSAR-2 is, thus, usable for disaster response with some inconsistencies which are explainable with the microwave characteristics. A post-event backscatter amplitude image is to be interpreted visually with assistance of other satellite images, if interferometric SAR technique cannot be used due to lack of pre-event archived data from the same orbit,. The visual interpretation needs careful examination by changing the brightness and contrast of the image, because microwave reflection is influenced simultaneously by both the physical properties and the geomorphic shape of the target area. Through this observation, we have recognized that the visual identification of an unknown hazard only using images is difficult. Therefore, we needed some information about the place and the type of hazard being investigated before interpretation so far. Nevertheless, the approximate scale of the collapse was successfully recognized and provided to the related authorities for emergency response.

Accumulation of the archived data more than once from each orbit enables the coherence normalization to emphasize the unusual coherence decrease by a hazard. Furthermore, removing the small patches by means of focal statistics successfully resulted in sediment extraction, which is reasonably consistent with that from a high-resolution satellite image. For other kind and scale of hazards, the parameter settings (i.e., circle size to obtain a mean value) needs to be assessed and validated

through several case studies. The NCD calculation cannot be used for slightly, but constitutively changing terrains, such as river banks and vegetation.

In terms of the avalanche source, we found two parts of high NCD values above the collapse sediment on the hillslope ((q) and (r) in Fig. 6b). On the glacier surfaces, regular flowing could de-emphasize the unusual change caused by the avalanche or other collapse events, even if they had happened. The two parts suggest that the falling materials went through these parts and altered their surface features. We could not detect the drastic surface changes in the uphill between AW3D (pre-event) and WV-3 (post-event) images, but Lacroix (2016) supported our suggestion by comparison of DSMs generated from Satellite Pour l'Observation de la Terre (SPOT). Such an extremely-steep slope is difficult to obtain an accurate DSM from most of satellite images, therefore NCD would be preferable focus to be coupled with DSM comparison.

4.2 Validation of volume estimation

Kargel et al. (2015) estimated total mass of this sediment as ~3.3×10^9 kg, assuming homogeneous thickness of 2 m on its entire surface. Our study revealed heterogeneous volume distribution, which is especially concentrated along the water streams. According to the assumed density of 2200 kg m^{-3} (Kargel et al., 2015), our estimated volume (5.51×10^6 m^3) turns out to be 12.1×10^9 kg, reaching 3.7 times of the former (Kargels') estimation. Our volume estimation is smaller than that by Lacroix (2016) through a comparison of SPOT-derived DSMs (6.95×10^6 m^3), possibly because the second avalanche was caused between 8 and 10 May (e.g. Fujita et al. 2016). Furthermore, Fujita et al. (2016) performed an in-situ survey from which they estimated the total volume of the first avalanche sediment as $6.81 \pm 1.54 \times 10^6$ m^3, covering our estimation value in the possible range.

4.3 Temporal sequence of the avalanche event

Identification of sediment deposition layers from the interpretation of a high-resolution WV-3 image suggests that different sources provided various types of deposition continuously in a short period (Fig. 3). Splashing feature of the group (A) denotes a uniformed scattering direction along lines (x) to (y), suggesting an origin around the cross point of the lines (Fig. 4a). The group (B) and (C) has a lighter similar color than that of (A) and range wider coverage along the line (z) without splashing (Fig. 4a). Thus a border between (A) and (C) is visually identifiable (p1 in Fig. 4b). Huge mass of (B) and (C) denoted in Fig. 6a implies slower continuous flowing, whereas negative altitude change on (A) implies fast scattering with air blast which mowed trees down with less mass deposited on the steep slope. These conclude that the group (B) was provided after deposition of (A) with slower speed and larger volume from a different source, which was terminated filling the riverbed in (C) at the end.

Closing up, the west side of the group (D) has a similar surface feature and gradual color similarity to (B) (p2 in Fig. 4e). In addition, the group (E) has a similar surface feature to that of (C) with some wrinkles with a different surface color. These suggests that the layers of (D) and (E) are much thinner layer than those of (B) and (C), and they rode the formerly deposited (B) and (C).

The group (F) is connecting to (D) and similar darker color to the detached group of (G) (Fig. 3). They seem to have smaller amount of mass deposition than (D) at the same or later time from different sources. There are distributed with many ununiformed apertures, implying vertical dropping from the source (possibly after hitting some headwall surfaces), rather than the fast second scattering after once hitting the ground terrain as seen on (A).

The group (H) is distinguished from (B) by its darker color (Fig. 4d) and the beginning headwall foot at the west side (Figs. 3; 4f). The group (I) have a narrow flow with a certain thickness (~10 m) (Table 1) originated from the westernmost part of (H). It is terminated at the river floor, where it pushes and displaces the snout of (C) (p3 in Fig. 4c). They suggest that (H) and (I) are accumulated later than (B) and (C) from another source.

The group (J) has many apertures with slight flowing (fig. 4f). Its lighter and darker colors than (H) is not related to the flow direction, that implies heterogeneous mixture of materials were supplied, possibly hitting and involving several origins along the headwall.

Consequently, these considerations give a perspective of temporal sequence that avalanche event provided multiple types of depositions in order of,

(A) with extremely fast speed with air blast,

(B) with less flowing speed which covers the entire surface from the hoot of the headwall to the river floor,

(C) as a stacking part of (B) with the least flowing speed along the river flow to the downstream and partially upstream, depositing huge mass,

(D) which covers the eastern part of (B) after its deposition with some splashing,

(E) as a terminal part of (D) which covers the eastern part of (C) with thin layer,

(F) and (G) with a relation to (D), with which splashing in a larger area implies dropping from relatively higher position,

(G) with which splashing feature implies experience of hitting the headwall before deposition,

(H) as the terminal part of (H), riding the terminus of (C) with muddy flowing.

The group (J) is an independent deposition from neighboring (H), however the deposition timing in the above sequence is unknown. In addition, the group (H) has a possibility of earlier deposition than (D) to (G), because the groups of (D) and (H) has no direct relationships in evidence.

The suggested sequence is applied on the vertical profiles of Figs. 6b and 6c, schematically illustrated in Figs. 6d and 6e. Multiple types of avalanche-induced sediments are deposited in layers. The initial sediment, (A) will exist under the following sediment of (B) to (C) along A-A', and additionally (D) to (E) along B-B'. An in-situ survey with boring core and/or ground penetration radar might give some supporting findings. Realistic numerical simulation of avalanche collapse and analysis of heat balance related to the melting process would need the consideration of multiple layers precisely mapped by our study. The muddy features interpreted in some layers imply high ice and snow content which are confirmed in an in-situ survey after the monsoon season (Fig. 9). Coupling further altitude measurements with temporal intervals would clarify the surface lowering by ice/snow melting, for which the water content estimation is invaluable as one of the input data for avalanche simulation and source consideration.

5 Conclusion

Initial multi-satellite observation and assessment were carried out for the catastrophic avalanche induced by the 2015 Gorkha Earthquake in Nepal on April 25. Radar observation by means of PALSAR-2 resulted in two successful ways of backscatter amplitude image and coherence analysis, which are both usable for urgent hazard response to acquire quantitative information, not hindered by frequent cloud cover in those regions during monsoon. Detailed visual interpretation and classification of the sediments with a WV-3 pan-sharpened image suggested multiple sediment layers, which suggest sequential failure of materials from different sources. The difference between the pre- and post-event DSMs estimated a total sediment volume of 5.51 $\times 10^6$ m^3 (12.1×10^9 kg as weight), of which the dominant mass is accumulated along the river streams. Negative altitude change suggests erosion and denudation of surface objects and measurement error in difficult topography for DSM generation. Quantitative spatial and volumetric assessments and classification derived from this study would contribute for further studies such as avalanche simulation and melting process estimation, e.t.c.

Author contribution

H. Nagai designed the total analysis and discussion. M. Watanabe carried out InSAR coherence calculation and improved the manuscript. N. Tomii organized use of WorldView-3 image. T. Tadono and S. Suzuki managed ALOS-2 observation.

Competing interests

The authors declare that they have no conflict of interest.

Acknowledgement

We greatly appreciate the financial support from the Council for Science, Technology, and Innovation (CSTI), Cross-ministerial Strategic Innovation Promotion Program (SIP), "Enhancement of societal resiliency against natural disasters" (Funding agency: Japan Science and Technology agency). WorldView-3 image was distributed by DigitalGlobe, Inc. WorldView-3 digital surface model was generated by NTTDATA CORPORATION, included DigitalGlobe, Inc. ALOS World 3D dataset was generated by NTTDATA CORPORATION and Remote Sensing Technology Center of Japan included JAXA. We thank Dr. K. Tsutsui, M. Ozaki, and their colleagues at NTT DATA CORPORATION Inc. for providing technical information. We also thank the members of J-RAPID team "Investigation of cryo-geohazards in Langtang Valley, Nepal" founded by the Japan Science and Technology Agency and those of a non-governmental organization, Langtang Plan, for valuable information from their post-hazard in-situ survey. We thank the editor and two anonymous reviewer for their valuable comments and handling of review process.

References

Arita, K., Ohta, Y., Akiba, C., and Maruo, Y.: Kathmandu region. In. Hashimoto, S. (ed.), Geology on Nepal Himalayas, Sapporo, Saikon Publishing, 99–145, 1973.

Ball, G. H. and Hall, D. J.: ISODATA, a novel method of data analysis and pattern classification, Stanford research institution, Menlo Park CA, 1965.

Fujita, K., Inoue, H., Izumi, T., Yamaguchi, S., Sadakane, A., Sunako, S., Nishimura, K., Immerzeel, W. W., Shea, J. M., Kayashta, R. B., Sawagaki, T., Breashears, D. F., Yagi, H., and Sakai, A.: Anomalous winter snow amplified earthquake induced disaster of the 2015 Langtang avalanche in Nepal, Nat. Hazards Earth Syst. Sci. Discuss., doi:10.5194/nhess-2016-317, in review, 2016.

Ge, L., Ng, A.H., Li, X., Liu, Y., Du, Z., and Liu, Q.: Near real-time satellite mapping of the 2015 Gorkha earthquake, Nepal, Ann. GIS, 21(3), 175–190, doi:10.1080/19475683.2015.1068221, 2015.

Goda, K., Kiyota, T., Pokhrel, R., Chiaro, G., Katagiri, T., Sharma, K., and Wilkinson, S.: The 2015 Gorkha Nepal earthquake: insights from earthquake damage survey, Front. Built. Environ. 1(8), 1–15, doi:10.3389/fbuil.2015.00008, 2015.

ICIMOD: Geohazards in the aftermath of the 25 April 2015 (12 Baisakh 2072) earthquake, A rapid analysis prepared for the Government of Nepal, 2015a. [http://www.icimod.org/?q=18072]

ICIMOD: Villages in Langtang Valley destroyed by landslides and pressure waves during the 25 April 2015 earthquake, 2015b. [http://www.icimod.org/?q=18314]

Kargel, J.S., Leonard, G.J., Shugar, D.H., Haritashya, U.K., Bevington, A., Fielding, E.J., Fujita, K., Geertsema, M., Miles, E.S., Steiner, J., Anderson, E., Bajracharya, S., Bawden, G.W., Breashears, D.F., Byers, A., Collins, B., Dhital, M.R., Donnellan, A., Evans, T.L., Geai, M.L., Glasscoe, M.T., Green, D., Gurung, D.R., Heijenk, R., Hilborn, A., Hudnut, K., Huyck, C., Immerzeel, W.W., Jiang, L., Jibson, R., Kaab, A., Khanal, N.R., Kirschbaum, D., Kraaijenbrink, P.D.A., Lamsal, D., Liu, S., Lv, M., McKinney, D., Nahirnick, N.K., Nan, Z., Ojha, S., Olsenholler, J., Painter, T.H., Pleasants, M., KC, P., Yuan, Q., Raup, B.H., Regmi, D., Rounce, D.R., Sakai, A., Shangguan, D., Shea, J.M., Shrestha, A.B., Shukla, A., Stumm, D., van der Kooij, M., Voss, K., Wang, X., Weihs, B., Wolfe, D., Wu, L., Yao, X., Yoder, M.R., and Young, N.: Geomorphic and geologic controls of geohazards induced by Nepal's 2015 Gorkha earthquake. Science, 351(6269), doi:10.1126/science.aac8353, 2015.

Kobayashi, T., Tobita, M., Koarai, M., Otoi, K., and Nakano, T.: Liquefaction Area Associated with the 2011 off the Pacific coast of Tohoku Earthquake, Inferred from Interferometric SAR Coherence Change, Journal of Geospatial Information Authority of Japan, 122, 143–151, 2011 (in Japanese).

López-Martínez, C. and Pottier, E.: Coherence estimation in synthetic aperture radar data based on speckle noise modeling. Applied optics, 46(4), 544–558, 2007.

Lacroix, P.: Landslides triggered by the Gorkha earthquake in the Langtang valley, volumes and initiation processes, Earth, Planets and Space, 68(46), doi:10.1186/s40623-016-0423-3, 2016.

Ono, Y. and Sadakane, A.: Natural background of the yak transhumance in the Langtang valley, Nepal Himalaya, Geographical Reports of Tokyo Metropolitan University, 21, 95–109, 1986.

Parameswaran, R.M., Natarajan, T., Rajendran, K., Rajendran, C.P., Mallick, R., Wood, M., and Lekhak, H.C.: Seismotectonics of the April–May 2015 Nepal earthquakes: An assessment based on the aftershock patterns, surface effects and deformational characteristics, J. Asian Earth Sci., 111, 161–174, doi:10.1016/j.jseaes.2015.07.030, 2015.

Plank, S.: Rapid damage assessment by means of multi-temporal SAR—A comprehensive review and outlook to Sentinel-1. Remote Sensing, 6(6), 4870–4906, 2014.

Richards, J. A.: Remote sensing digital image analysis: An Introduction, Berlin: Springer, 1999.

Roy, B., Sathian, B., and Banerjee, I.: Nepal earthquake 2015–an overview, J. Biomed. Sci., 2(1), 1–2, doi:10.3126/jbs.v2i1.13030, 2015.

Shiraiwa, T. and Watanabe, T.: Late Quaternary glacial fluctuations in the Langtang Valley, Nepal Himalaya, reconstructed by relative dating methods, Arctic Alpine Res., 23(4), 404–416, doi:10.2307/1551682, 1991.

Shiraiwa, T.: Glacial fluctuations and cryogenic environments in the Langtang Valley, Nepal Himalaya. Contributions from the Institute of Low Temperature Science. Series A, 38, 1–98, 1994.

Tadono, T., Takaku, J., Tsutsui, K., Oda, F., and Nagai, H.: Status of "ALOS World 3D (AW3D)" global DSM generation, Proc. of Geoscience and Remote Sensing Symposium (IGARSS), 2015 IEEE International, 3822–3825, 2015.

Tamura, M. and El-Gharbawi, T.: Mapping damage in Shinomaki City due to the 2011 Tohoku Earthquake using InSAR coherence change, Proc. of the 58th Spring Conference of the Remote Sensing Society of Japan, 29–30, 2015 (in Japanese).

Yonezawa, C. and Takeuchi, S.: Decorrelation of SAR data by urban damages caused by the 1995 Hyogoken-nanbu earthquake, Int. J. Remote Sens., 22(8), 1585–1600, 2001.

Touzi, R., Lopes, A., Bruniquel, J., and Vachon, P. W.: Coherence estimation for SAR imagery. IEEE Transactions on Geoscience and Remote Sensing, 37(1), 135–149, 1999.

Watanabe, M., Thapa, R. B., Ohsumi, T., Fujiwara, H., Yonezawa, C., Tomii, N., and Suzuki, S.: Detection of damaged urban areas using interferometric SAR coherence change with PALSAR-2. Earth, Planets and Space, 68(1), 131, 2016.

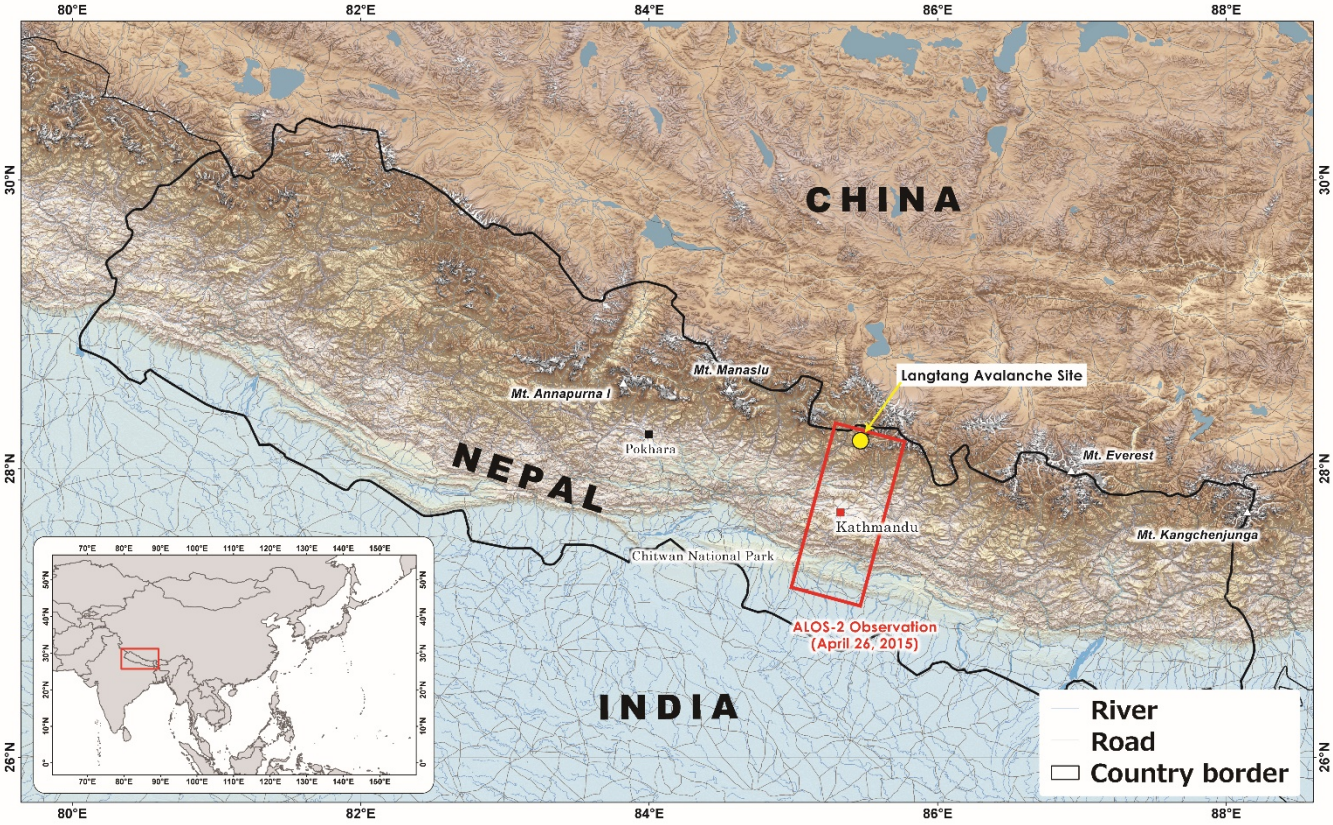

Figure 1: Location of the study site. Topography obtained from NASA/USGS SRTM3v4, glacier outlines obtained from ICIMOD Mountain Geoportal, rivers and roads obtained from DIVA-GIS, and country borders obtained from ThematicMapping.org are illustrated.

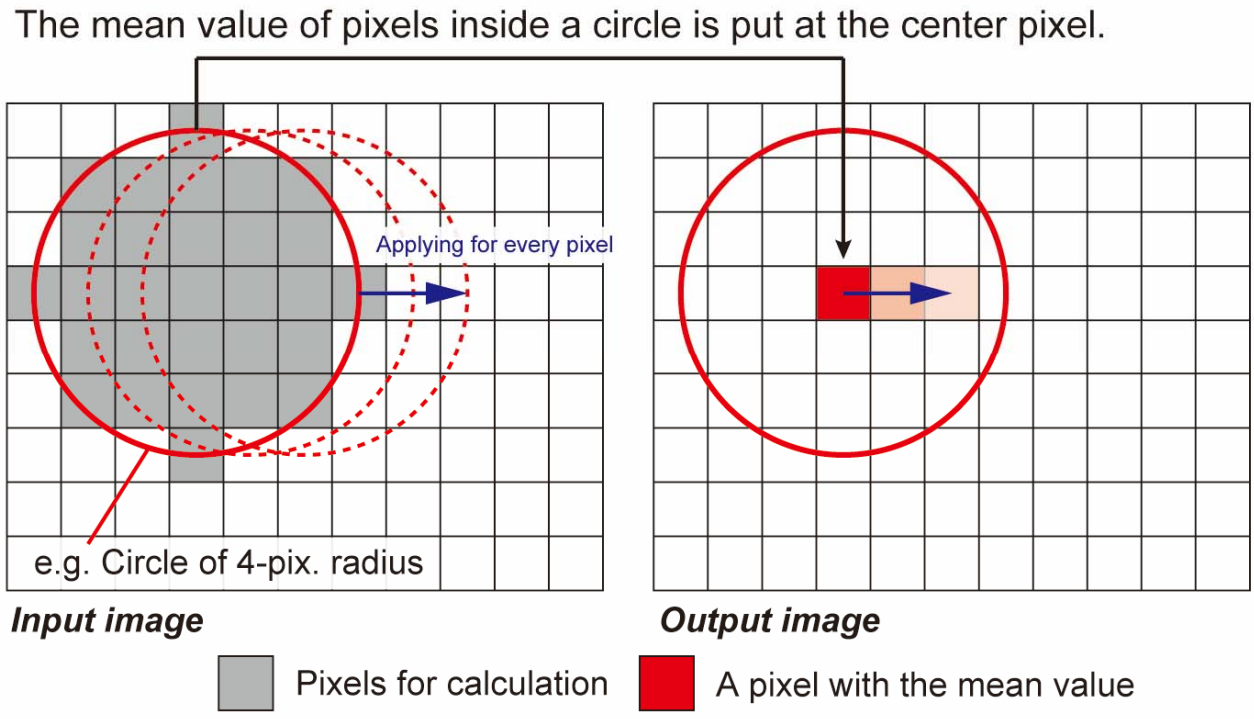

Figure 2: Concept of focal statistics filter to reduce noises.

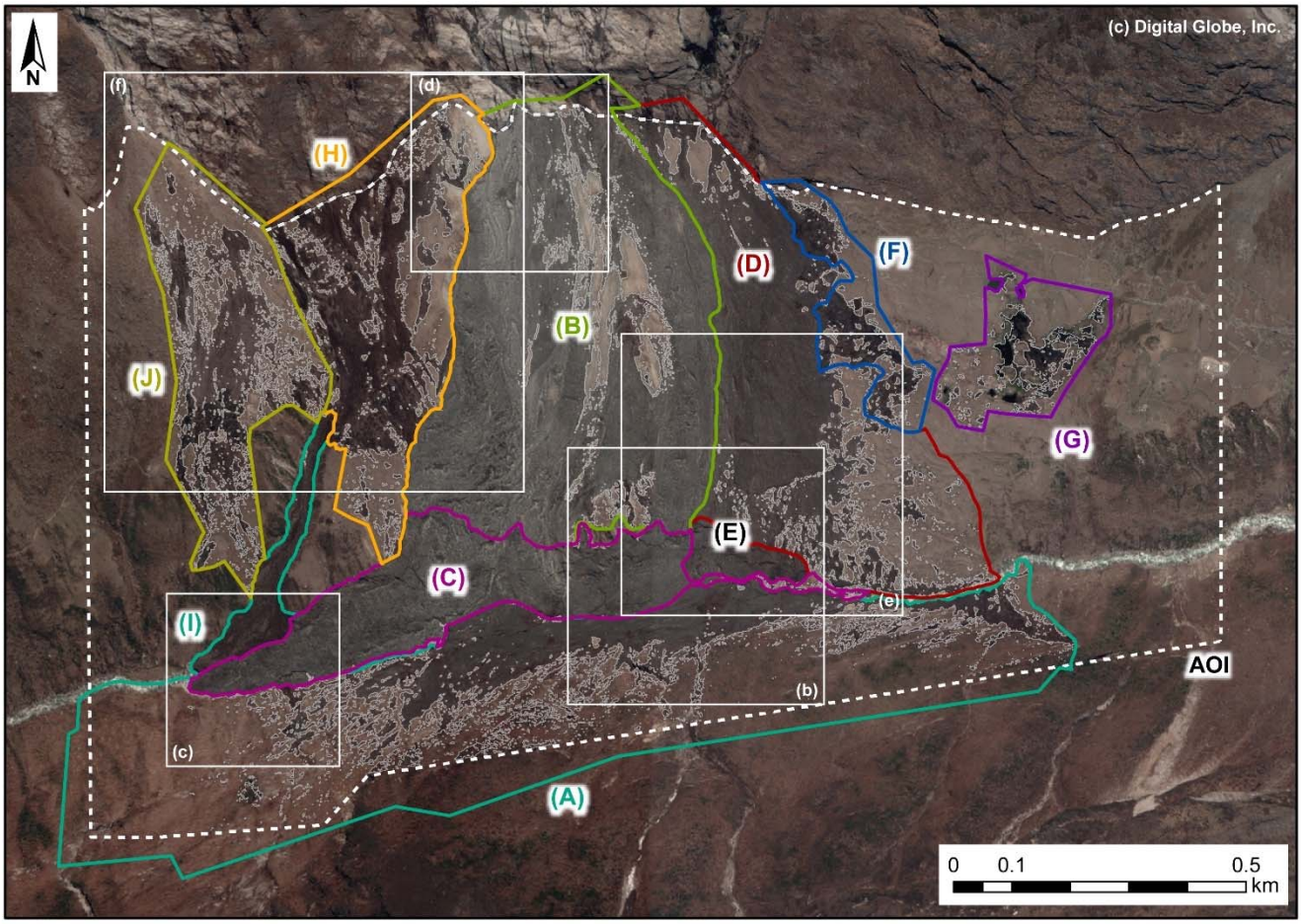

Figure 3: **Avalanche-induced sediment deposition observed with World View-3. A dot rectangle is the area of interest (AOI) of this study, within which sediment depositions are classified from (A) to (J). Squares are corresponding to the closed-up view in Fig. 4.**

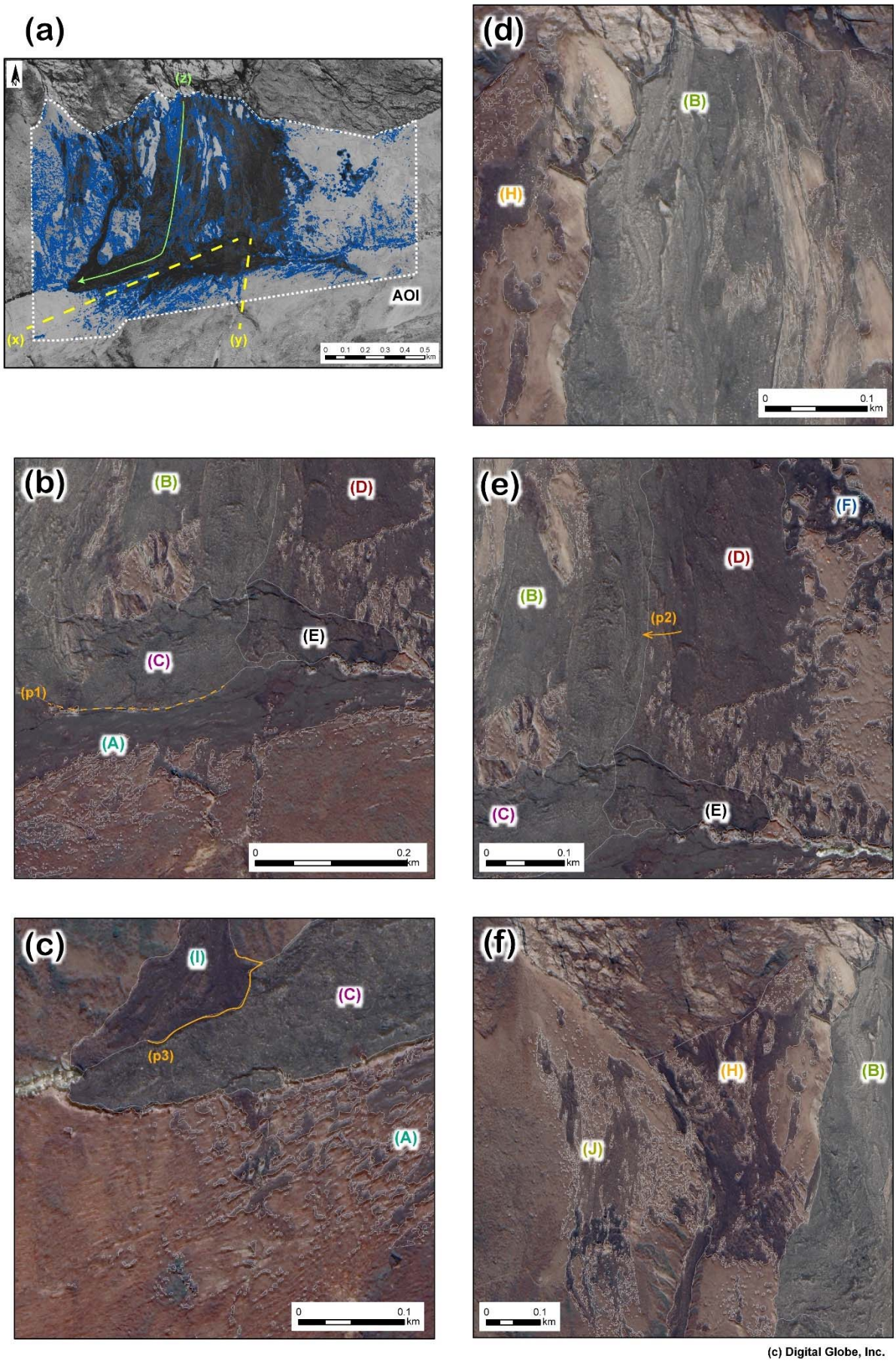

Figure 4: **Details of sediment mapping. (a) Un-supervised classification was initially applied on the WV-3 thermal infrared image. (b-f) detail interpretation and classification was carried out comparing the differences of sediment colors and physical characteristics.**

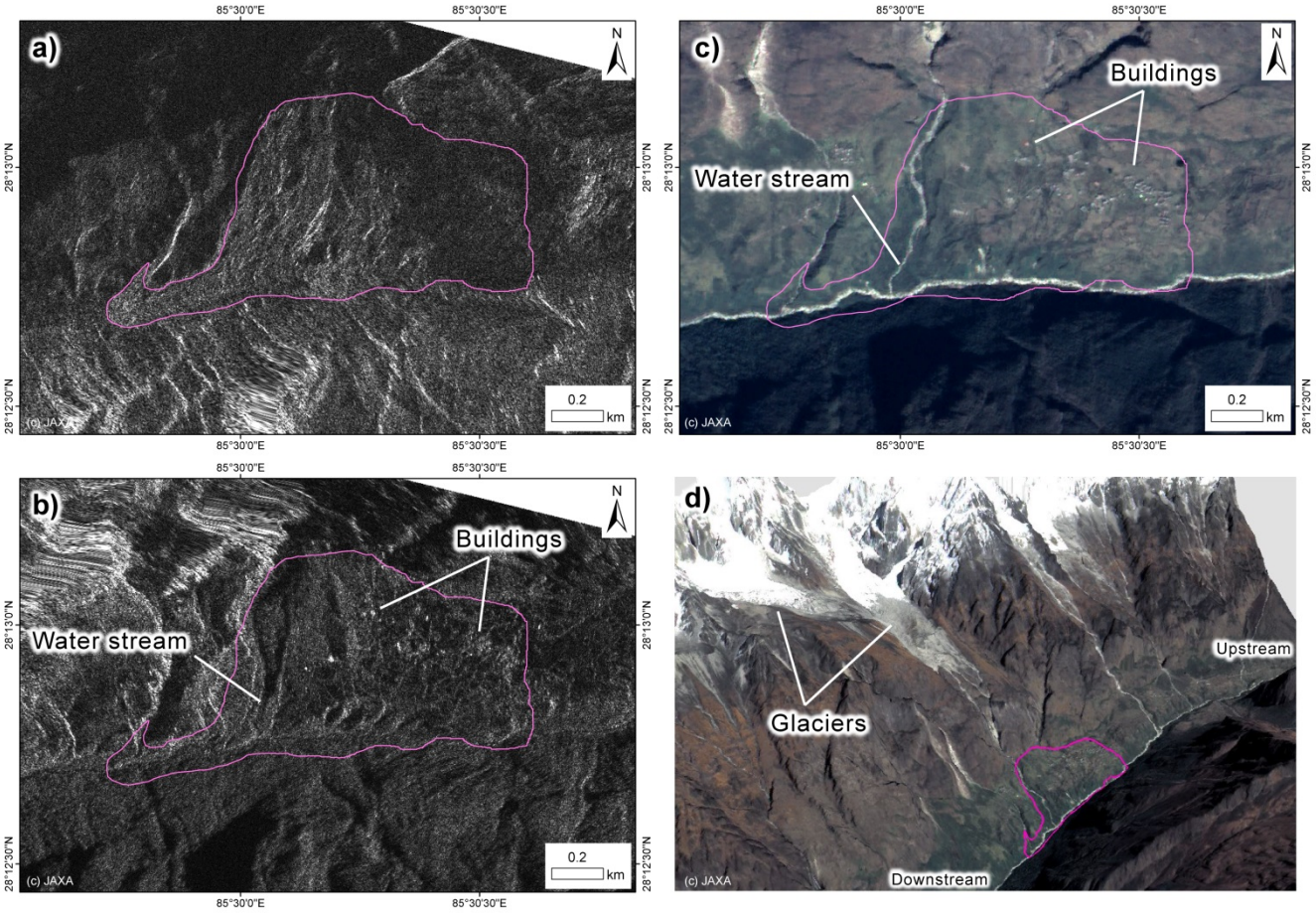

Figure 5: Identified collapsed sediment by ALOS/ALOS-2 images. Difference between PALSAR-2 images of (a) post-quake (April 26, 2015) and (b) pre-quake (December 28, 2014) denotes that the buildings and water stream identifiable by (c) a pre-quake ALOS pan-sharpened image (October 12, 2008) has been covered by the sediments. (d) A three-dimensional view of the ALOS pan-sharpened image overlaid on ALOS World 3D digital surface model.

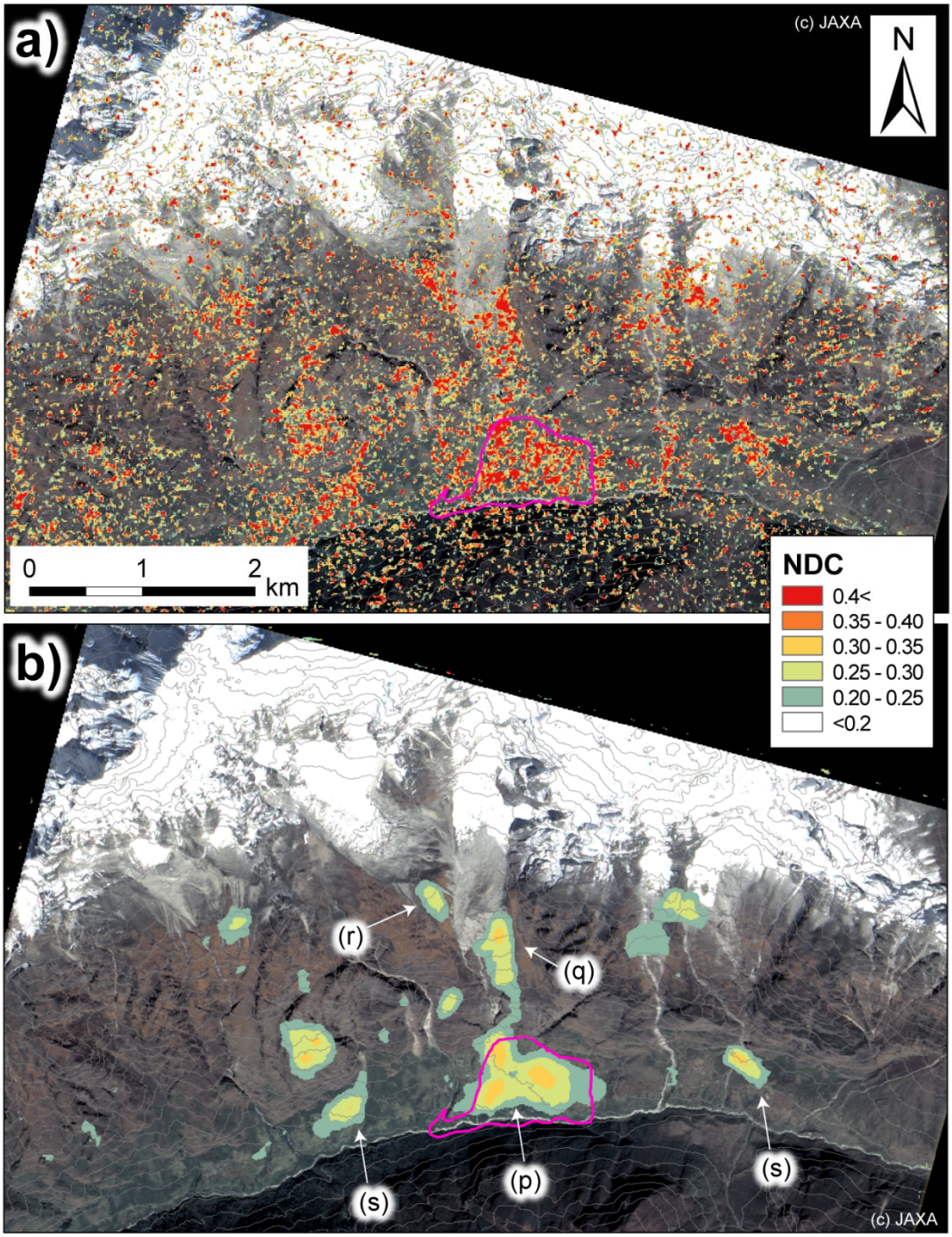

Figure 6: Normalized coherence decrease around the collapsed area in Langtang Valley. (a) Original output image is processed into two images of focal statistics with (b) 15-m circles for calculating the mean values. High-value parts are denoted on (p) the collapse area, (q) a glacier moraine, and (r) that of a tributary glacier, as well as (s) two places in the valley bottom. The background is an ALOS pan-sharpened image observed on October 12, 2008.

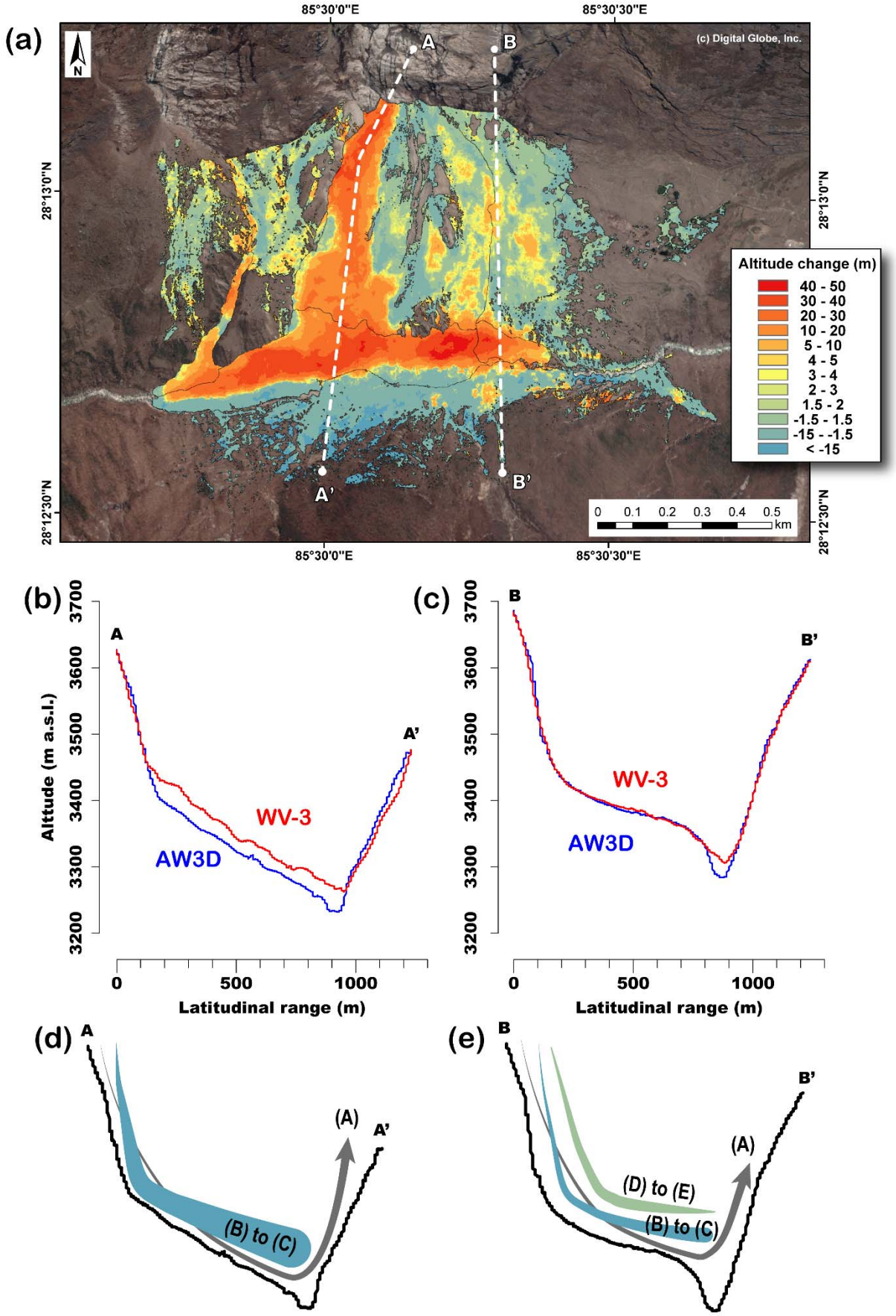

Figure 7: (a) Estimation of the sediment volume from the altitude difference between pre-event ALOS World 3D DSM and post-event WV-3 DSM. Vertical profiles along (b) A-A' and (c) B-B' are used respectively for (d) (e) schematic illustration of avalanche sequences.

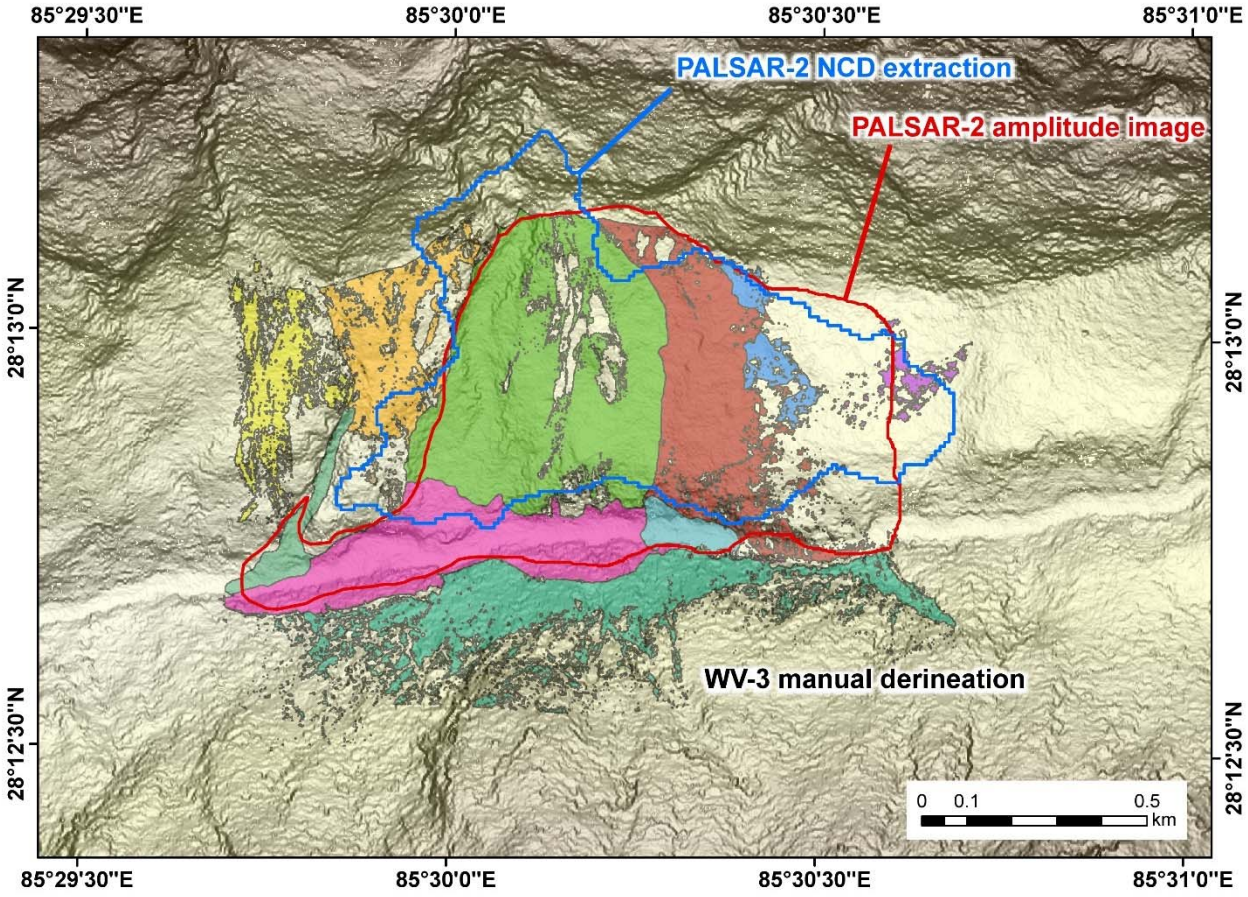

Figure 8: Sediment outlines delineated from PALSAR-2 data and WorldView-3 (WV-3) imagery. The background is hill-shade imagery generated from the AW3D DSM.

Figure 9. (a) A picture on the avalanche-induced sediment surface taken in an in-situ survey carried out for/by Fujita et al. (2016). (b) A closed-up picture showing exposed and melting ice. [Date: Oct. 21, 2015]

Table 1: Identifiable surface color-and-physical features, area, thickness, and volume changes for the 10 classified deposition groups.

Group	Colour	Surface feature	Area (km^2)	Altitude change (m)		Volume change (10^6 m^3)								
				Average	Mean	Deposition			Erosion			Net		
(A)	Dark	Muddy to splash	0.16	28.1	-9.3	0.09	±	0.02	1.14	±	0.15	-1.05	±	0.15
(B)	Light	Flowing with streaks	0.25	42.9	7.5	1.99	±	0.23	0.11	±	0.05	1.88	±	0.24
(C)	Light	Muddy	0.13	46.4	17.8	2.53	±	0.15	0.17	±	0.03	2.36	±	0.16
(D)	Dark, gradually light	Less flowing and few streaks	0.14	23.8	0.5	0.13	±	0.06	0.07	±	0.04	0.06	±	0.07
(E)	Dark, gradually light	Muddy	0.02	41.7	19.7	0.30	±	0.02	0.00	±	0.00	0.30	±	0.02
(F)	Very dark	Muddy and splash	0.02	3.7	-1.8	0.00	±	0.00	0.03	±	0.02	-0.03	±	0.02
(G)	Very dark	Detached, muddy and splash	0.01	1.4	-1.7	0.00	±	0.00	0.01	±	0.01	-0.01	±	0.01
(H)	Dark	Muddy and splash	0.07	39.2	1.3	0.09	±	0.04	0.04	±	0.02	0.06	±	0.04
(I)	Dark	Muddy	0.02	30.6	10.5	0.21	±	0.03	0.00	±	0.00	0.20	±	0.03
(J)	Light to dark	Muddy and splash	0.05	13.2	1.4	0.05	±	0.02	0.01	±	0.00	0.04	±	0.02
Total			**0.88**	**46.4**	**4.0**	**5.51**	**±**	**0.09**	**1.64**	**±**	**0.06**	**3.87**	**±**	**0.11**